



## Article

# Effect of Substrate Bias Voltage on Microstructure and Mechanical Properties of Cr-Nb-Ti-Zr-N-O Ceramic Thin Films Produced by Reactive Sputtering

Sayed Alireza Ataie<sup>1</sup>, S. Mahmoudi Qashqay<sup>2</sup>, Mohammad Reza Zamani-Meymian<sup>2,\*</sup>  and Fabio Ferreira<sup>3,4</sup> 

<sup>1</sup> School of Metallurgy and Materials Engineering, Iran University of Science and Technology (IUST), Narmak, Tehran 16846-13114, Iran; ata.sayedalireza@gmail.com

<sup>2</sup> Physics Department, Iran University of Science and Technology (IUST), Narmak, Tehran 16846-13114, Iran; asamanehmahmoudi@gmail.com

<sup>3</sup> Department of Mechanical Engineering, ARISE, CEMMPRE, University of Coimbra, Rua Luís Reis Santos, 3030-788 Coimbra, Portugal; fabio.ferreira@dem.uc.pt

<sup>4</sup> Laboratório de Ensaios Desgaste e Materiais, Instituto Pedro Nunes, LED&Mat-IPN, Rua Pedro Nunes, 3030-199 Coimbra, Portugal

\* Correspondence: r\_zamani@iust.ac.ir

**Abstract:** Hard coatings are applied in various applications to protect substrates from wear and corrosion. In the present study, multi-element ceramic films are deposited by reactive sputtering. The level of substrate bias voltage (−50, −125 and −200 V) is changed to investigate the structural and mechanical properties of Cr-Nb-Ti-Zr-N thin films. Chemical analysis (using EDS, XRD and Raman spectroscopy) reveals that these thin films (with a high amount of oxygen) are composed of a nanocomposite phase structure (amorphous and nano-crystalline phases). CrO<sub>2</sub> and Nb<sub>x</sub>N crystalline phases exist in an amorphous matrix in the coatings. By increasing the substrate voltage (from −50 to −200 V), the nitrogen content (from 30 to 40 at. %) increases, and Cr<sub>x</sub>N crystalline phases are generated in S125 and S200. Morphological, topological and image analysis (employing FESEM and AFM) data show that the intermediate level of substrate bias voltage (sample S125) can produce a uniform surface with minimum defect density (15%). In addition, S125 has the minimum level of roughness (16.6 nm), skewness (0.2) and kurtosis (2.8). Therefore, the hardness, toughness and wear resistance (extracted from indentation and scratch tests) of this sample is maximum (H is 24.5 GPa and H/E is 0.107), while sample S50 shows complete fracture and delamination.

**Keywords:** thin film; ceramic coating; fractal parameters; indentation; scratch



**Citation:** Ataie, S.A.; Qashqay, S.M.; Zamani-Meymian, M.R.; Ferreira, F. Effect of Substrate Bias Voltage on Microstructure and Mechanical Properties of Cr-Nb-Ti-Zr-N-O Ceramic Thin Films Produced by Reactive Sputtering. *Coatings* **2023**, *13*, 1141. <https://doi.org/10.3390/coatings13071141>

Academic Editor: Andrey V. Osipov

Received: 22 May 2023

Revised: 11 June 2023

Accepted: 18 June 2023

Published: 24 June 2023



**Copyright:** © 2023 by the authors. Licensee MDPI, Basel, Switzerland. This article is an open access article distributed under the terms and conditions of the Creative Commons Attribution (CC BY) license (<https://creativecommons.org/licenses/by/4.0/>).

## 1. Introduction

Multi-component coatings are highly used in various fields such as photovoltaic, gas sensing and especially machining industries to protect metallic tools. Furthermore, to have better performance in machining (e.g., die machining and cutting tools applications), ceramic thin films are preferred rather than metallic ones [1–6] due to the high hardness, thermal stability, chemical inertness and low thermal coefficient of ceramic materials [7–9]. Transition metal nitrides (TMNs) and transition metal carbides (TMCs) are the first choices to employ in related industries. Generally, it is recorded that TMCs have lower toughness than TMNs [10–12]. Hence, it is advisable to use TMNs in protective coatings. So far, the promising and prevalent systems which can satisfy these conditions are Ti-M1-M2-N and Cr-M1-M2-N (M1 and M2 are metals) [13–17]. To some extent, Cr-N thin film is preferable to Ti-N coatings because of its high corrosion and high-temperature oxidation resistance [18,19]. However, the low hardness of this system is a real challenge in tribological applications. Multilayering design (such as CrN/W<sub>2</sub>N, CrN/Mo<sub>2</sub>N and CrN/CrAlN) is one way to increase the hardness, but controlling and optimizing the bilayer number and thickness is a real challenge to achieve. Therefore, adding elements (such as Nb, Zr and Ti) is a better

offer to enhance the hardness [20–23]. Although the authors studied Cr-Zr-Nb-N systems previously [24], the role of adding more elements (such as Ti) at the same time or oxygen percentage in Cr-N thin films has not been reported yet.

Multi-element thin films can be produced in medium-entropy (if the system has four elements) and high-entropy (if the system has more than four elements) forms. However, it is extremely important to develop the coatings in defectless and nanostructure form to present the best performance [25–28]. Generally, reactive sputtering is a beneficial process to gain high-quality coatings. To control and design the microstructure of thin films, one can alter the substrate temperature [29,30], reactive gas type or content [31,32], substrate bias voltage [33–36] and target power [37,38]. Furthermore, it is important to investigate the effect of these parameters on mechanical properties. To add to it, the optimum conditions and properties should be obtained. Approximately, the optimum level of the sputtering factors was revealed for traditional thin films (two/three-element systems) previously. For example, the substrate temperature ( $T/T_m$ ) should be kept at an intermediate level. If it is too low, an amorphous with columnar/porous structure is obtained (which is hazardous for tribological properties) [39], and if it is too high, a large grain size is obtained and energy costs can be increased (which is not desirable) [40]. Likewise, the substrate bias voltage and peak power should be fixed at an intermediate value to produce high-energy particles with high deposition rates simultaneously [33–35,37]. In addition, it is suggested to set an intermediate level for the nitrogen-to-argon flow rate ratio in order to achieve higher hardness [32,41,42]. Because if it is too high, target poisoning happens, and if it is too low, nitride crystalline phases cannot be created adequately. Despite these explanations, the effect of substrate bias voltage on the structural and mechanical properties of Cr-Nb-Zr-Ti-N ceramic films has not been published yet.

The present study investigates the chemistry, morphology, topography and nanomechanical properties of Cr-Nb-Ti-Zr-N-O ceramic films. By changing the substrate bias voltage from  $-50$  to  $-200$  V, the oxygen content, fractal parameters and defect density are analyzed. Then, the relative hardness, toughness parameters and wear characteristics (friction coefficient, wear width and depth) are presented.

## 2. Materials and Methods

### 2.1. Coatings Preparation

To deposit Cr-Nb-Ti-Zr-N thin films, the sputtering chamber with three targets was employed. Two of them are DC (Cr and Nb have the percentage purity of 99.9%), and the other one is RF (half Ti and half Zr with the percentage purity of 99.9%). In the case of DC targets, the powers were fixed at 150 W, and in the case of RF source, the power was set at 200 W. The gases used in the runs are pure nitrogen (as the reactive gas) and argon (as the plasma gas). The gas ratio ( $N_2/Ar$ ) was 0.7 for all depositions. To analyze the structural and mechanical properties of the coatings, the substrate bias voltage was changed from low to high level ( $-50$ ,  $-125$  and  $-200$  V). The substrate temperature was fixed at  $380$  °C, and the working pressure was  $3 \times 10^{-2}$  Torr. In addition, the other sputtering parameters are fixed and are similar to the previous work of the authors [24].

### 2.2. Characterization Analysis

The phase structures of Cr-Nb-Ti-Zr-N coatings are analyzed by grazing incidence XRD (Bruker, D8 advance, Mannheim, Germany). The incidence angle was set at  $1^\circ$ , and the  $\lambda$  is  $1.54$  Å. The bond structure of the films is studied by Raman spectroscopy (Uni, DRON, Seoul, South Korea). The Ar-ion laser was  $457$  nm, and the resolution is  $1$   $cm^{-1}$ . The FESEM of VEGA-TESCAN was applied to investigate the morphology of the coatings. The acceleration voltage (from  $10$  to  $15$  kV) and work distance (from  $11$  to  $14$  mm) were varied. Both secondary electron and back-scattered electron detectors were applied to present the high-quality images. In addition, EDS was used to extract the elemental percentages of thin films. AFM images of thin films are presented by using atomic force microscopy of Ara Co., Tehran, Iran. Additionally, to drive fractal parameters, Gwyddion

software (version 2.60) was applied. The mechanical properties of the layers were noted by a nano-indentation/scratch set-up (Hysitron Inc. Triboscope, Minneapolis, Minnesota, United States) and Vickers tester (load is 50 g). Ten measurements (5 mN) were made for each coating to obtain the hardness and elastic modulus values. Five runs (from 1 mN to 8 mN) were completed to see the scratch behavior and scar of the films. To see indents' characteristics, a NanoScope III (from Digital Instruments, Tonawanda, New York, United States) was employed.

### 3. Results and Discussion

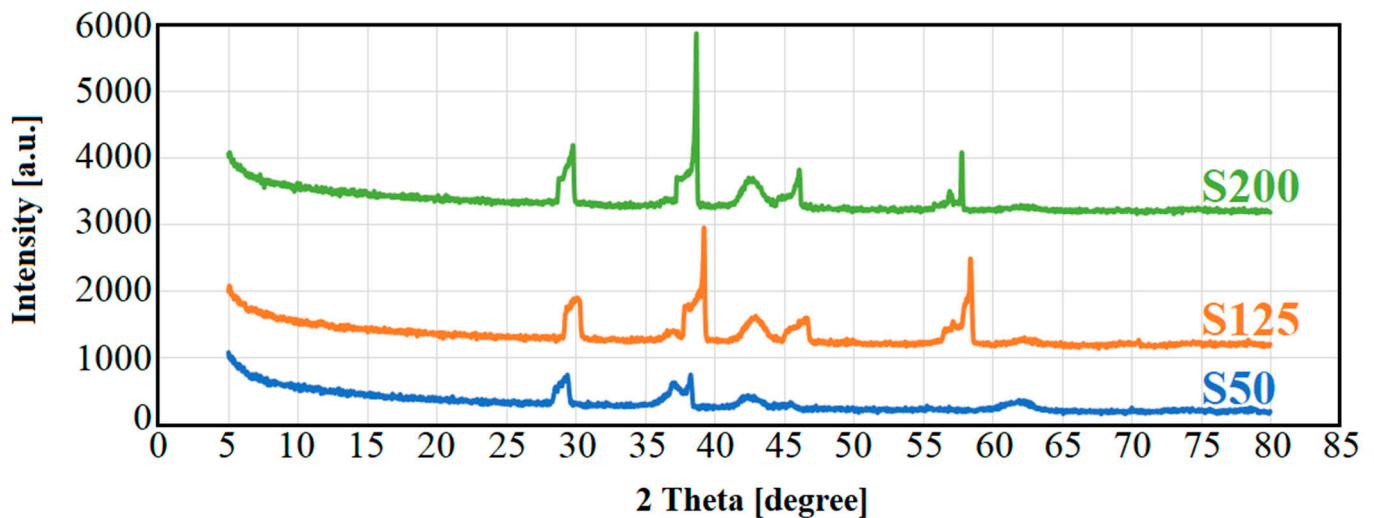
#### 3.1. Chemical Analysis

Table 1 indicates the elemental percentage of Cr-Nb-Ti-Zr-N thin films based on EDS results. It can be seen that by increasing the substrate bias voltage, non-metallic (N and O) elements vary significantly where the levels of metallic elements are nearly similar (for each element, the variation is lower than 2.7 at. %). Cr and Nb species received more at the growing coating because they are individual targets. However, in the case of Ti and Zr, they achieved lower amounts because they have a half-section target. Oxygen is a famous impurity in thin films produced by sputtering [2,29] if the content is lower than 6 at. %. However, because of the inadequate vacuum or residual gas and ambient air [43], in the present experiments, the oxygen percentage is high enough (more than 8.6 at. %) to assume as a principal component. Other studies [1,13] confirm this result. Therefore, the system should be called Cr-Nb-Zr-Ti-N-O. In addition, it must be mentioned that other impurities (such as argon, hydrogen and carbon) have low percentages (lower than 0.4 at. %) in the coatings.

**Table 1.** Elemental percentage of thin films based on EDS analysis.

Sample Code	Cr (at. %)	Nb (at. %)	Ti (at. %)	Zr (at. %)	N (at. %)	O (%)
S50	24.4	22.0	7.5	2.9	30.3	12.5
S125	22.6	19.3	6.8	2.5	40.1	8.6
S200	23.1	21.8	8.3	3.4	33.1	10.1

Figure 1 illustrates the X-ray patterns of Cr-Nb-Ti-Zr-N-O thin films. It is obvious that the composite phase structure (amorphous phase with crystalline phases) is gained in all coatings. Nevertheless, it is evident that increasing the bias voltage can increase the crystalline phases and content. In the case of S50, low-content crystalline phases are composed of CrO<sub>2</sub> (Ref. Code = 96-151-6111) and NbN (Ref. Code = 96-900-8684), where an amorphous phase is major. By increasing the substrate bias voltage and energy of the receiving particles [44], crystallinity is enhanced. In the case of S125, CrO<sub>2</sub> (Ref. Code = 96-151-6111), Cr<sub>2</sub>N (Ref. Code = 96-431-1895) and Nb<sub>2</sub>N (Ref. Code = 96-101-0511) crystalline phases are generated. The crystalline phases in S200 are CrO<sub>2</sub> (Ref. Code = 96-151-6111), CrN (Ref. Code = 96-100-8957) and Nb<sub>2</sub>N (Ref. Code = 96-101-0511). To explain more, based on the Scherrer equation, the crystallite size is 16.8 nm, 28.1 nm and 32.3 nm for S50, S125 and S200, respectively. Hence, it is obvious that nanocomposite coatings are produced by the sputtering process.



**Figure 1.** GI-XRD diffractograms of thin films.

Figure 2 shows the Raman spectra of Cr-Nb-Zr-Ti-N-O layers. It is clear that the peaks of the vibration frequencies in  $482$  and  $821\text{ cm}^{-1}$  are attributed to the Nb-N and Cr-O bonds, respectively. Moreover, there is a small peak at  $1100\text{ cm}^{-1}$  indicating the Cr-N bonds for all samples. These peak locations are in good agreement with the related studies [24,45]. By enhancing the substrate bias voltage, it is evident that the intensities of Cr-N and Cr-O peaks increase to a slight extent, but the intensity of Nb-N bonds increases notably. This result is in accordance with the XRD patterns in Figure 1. However, the abovementioned phase structure is not precise, and unknown amorphous phases (such as Ti-O-N) can exist in the coatings. Further study and XPS/TEM analysis can be useful to investigate more.

### 3.2. Morphological Analysis

Figures 3 and 4 show the cross-sectional and top-view morphologies of Cr-Nb-Ti-Zr-N-O thin films, respectively. It can be seen from Figure 3a,c that a columnar structure is dominant in S50 and S200. Moreover, this feature can produce micro-voids in thin films (see the green insets in Figure 3a',c'). Inversely, S125 shows a compact and featureless morphology. However, tiny columns and small voids are created and can be detectable by the green inset in Figure 3b'. Furthermore, the measured thickness of each coating is written in Figure 3a–c. As the deposition time was kept constant for all runs, it can be concluded that the deposition rate is maximum for low voltage (S50) and minimum for intermediate voltage (S125). Figure 4a–c indicate that if the plasma energy increases (by increasing the substrate bias voltage from low levels to higher than  $125\text{ V}$  [44]), atoms/ions diffuse more at the surface. Therefore, macro-grains and macro-particles cannot be created. The macro-particles created in S50 are presented by blue arrows in Figure 4a. Macro-particles and micro-voids are major defects in PVD hard coatings [25], so technological solutions should be applied to omit them. In order to determine the grain shape of the coatings, higher-resolution SEM images are represented in Figure 4a'–c'. As can be seen, S50 and S200 indicate no particular shape, and the grains are separated from each other (green insets in Figure 4a,c' obviously show the separation). In addition, the grain size of S50 is not identical in all the sites, and its grain shape is mixed of lamellar, oblique sheets and pyramids. In the case of S200, although the grain size is similar, the grain shape has cauliflower and island characteristics. Furthermore, Figure 4b' shows that the grain shape of S125 is rice-like, and its grain size is small and identical all over the specimen.

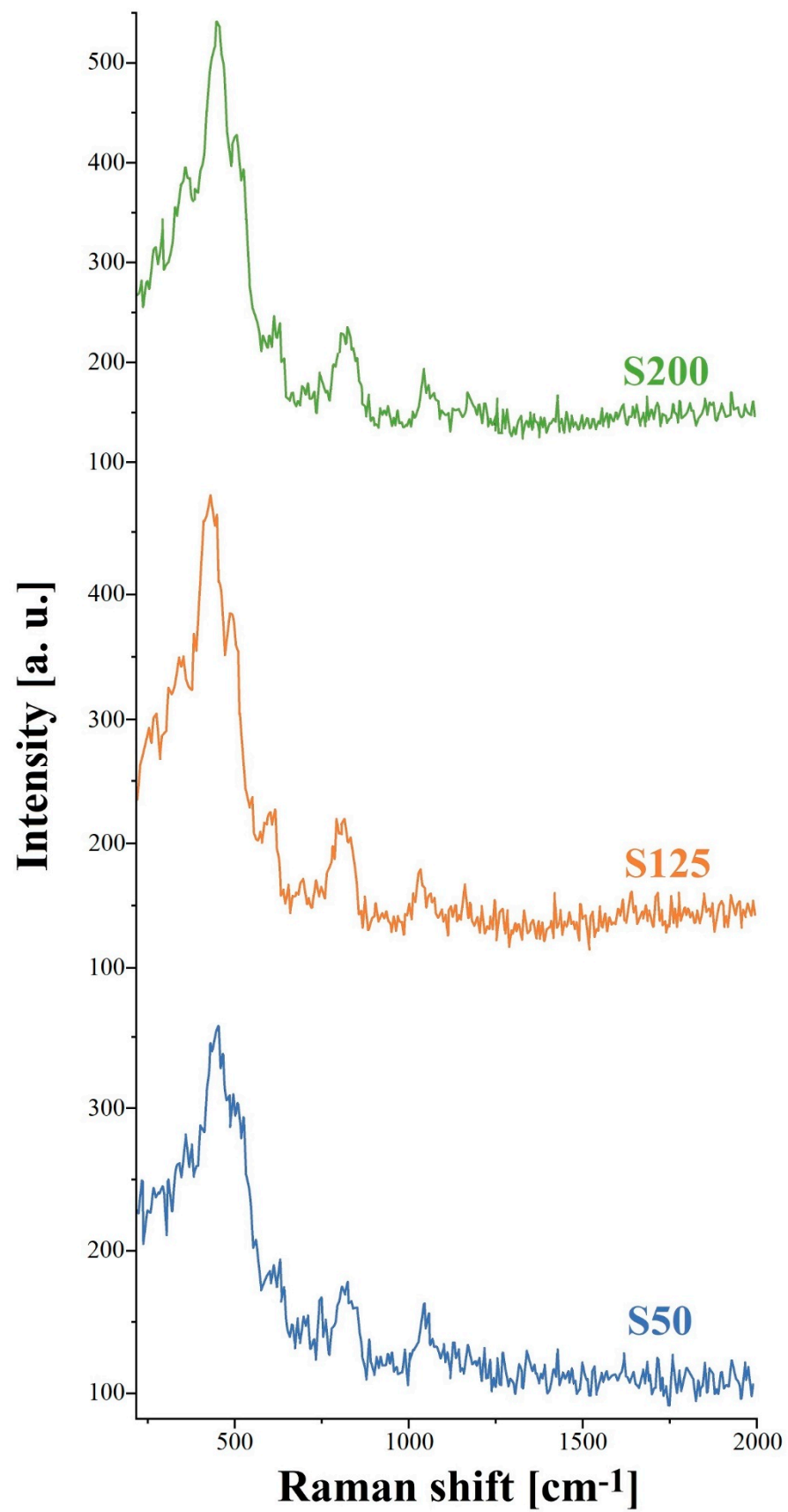
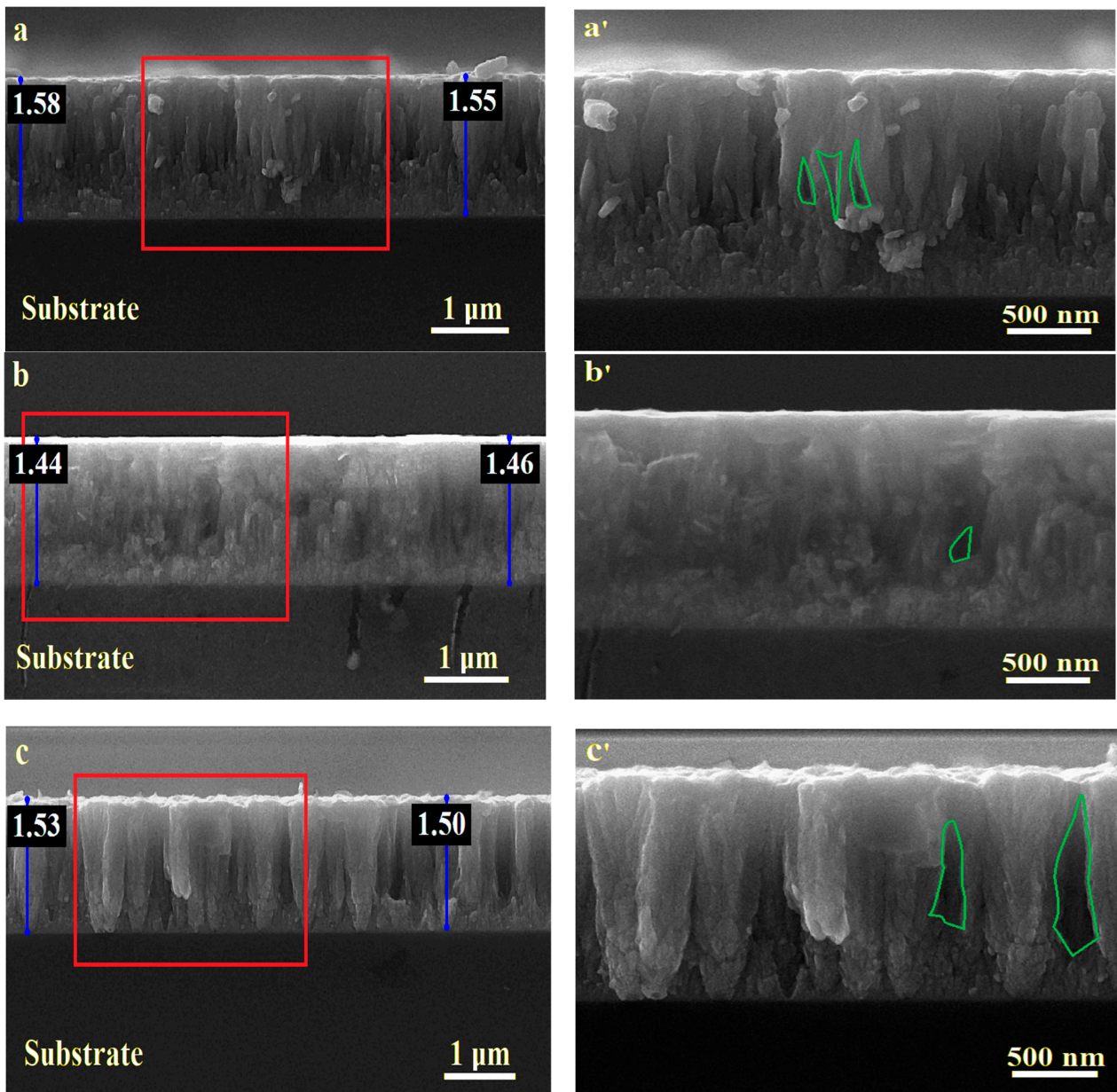


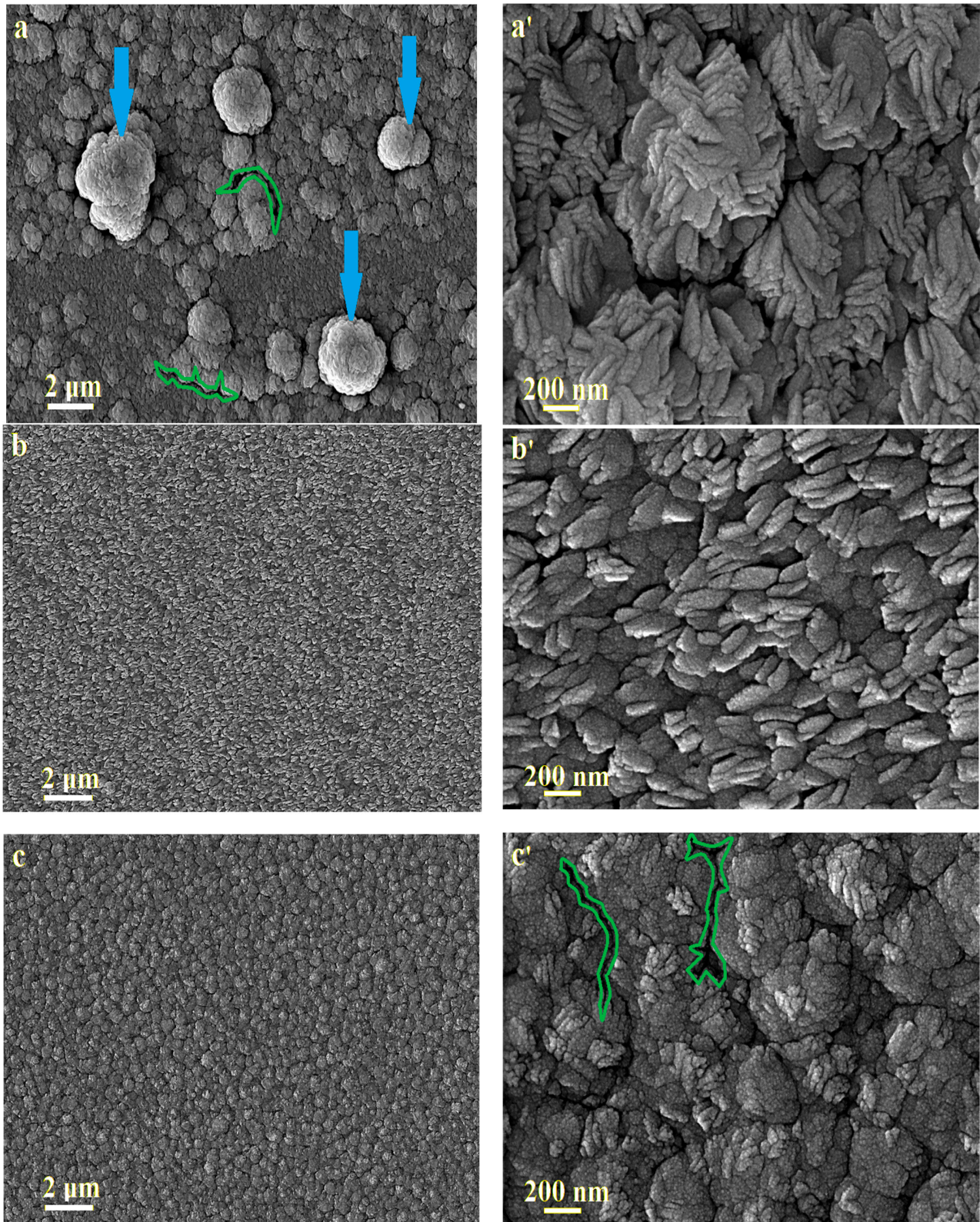
Figure 2. Raman spectra of thin films.



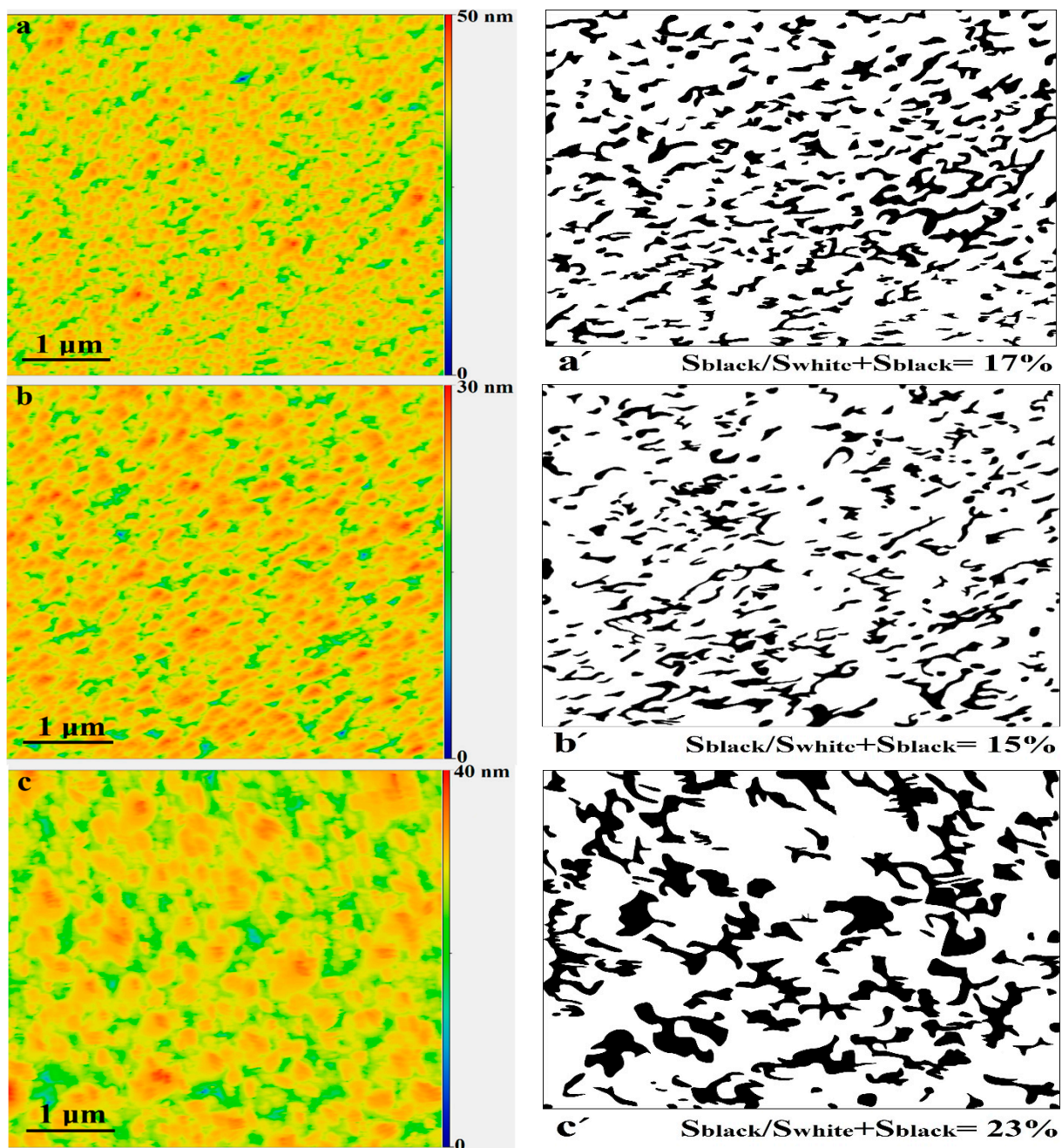
**Figure 3.** Cross-sectional SEM images of thin films; (a,a') S50, (b,b') S125 and (c,c') S200 (prime sections show red insets with higher magnification and pores).

Figure 5 shows 2D-AFM and binary images (extracted from the AFM images by the image analysis method) of Cr-Nb-Ti-Zr-N-O coatings. As can be seen, micro-voids (open boundaries at the surface of the coatings which are drawn by black areas) are minimum in S125 (15%). However, to analyze S50 and S200, the other surface defects (macro-particles) must be accounted for. To estimate the total defect density (micro-voids and macro-particles at the same time [25]), the authors assumed that dome-like macro-particles (see Figure 4a) are created and the circle area of macro-particles was accounted. Hence, the average calculated area of macro-particles for 5  $\mu\text{m}$  scale S50 images (such as the 2D AFM image) is 14%, and its total defect density is 31% (17% from Figure 5a' and 14% from Figure 4a). In addition, from AFM results, one can extract surface fractal parameters by graphical software [24,33]. Table 2 summarizes the data of average roughness (Ra), root mean square roughness (Rq), skewness (Sk), kurtosis (Ku) and fractal parameter (D). To study the detailed description and definition of these factors and their effects on friction, the reader is advised to see the literature [46,47]. As can be seen, D is similar for all layers. So, to study

surface geometry of the coatings, other parameters must be regarded. Maximum levels of Ra, Rq, Sk and Ku belong to sample S50, while the minimum levels are observed in the case of S125.



**Figure 4.** Low and high-magnification top-view SEM images of thin films: (a,a') S50, (b,b') S125 and (c,c') S200 (prime sections show higher magnification).



**Figure 5.** AFM and binary images of thin films; (a,a') S50, (b,b') S125 and (c,c') S200 (prime sections show valleys/open boundaries in black color).

**Table 2.** Fractal parameters of thin films based on AFM images.

Sample Code	Ra (nm)	Rq (nm)	Sk (-)	Ku (-)	D (-)
S50	20.2	23.7	-0.5	3.5	2.3
S125	13.5	16.6	-0.2	2.8	2.3
S200	19.2	21.4	-0.4	3.2	2.2

### 3.3. Mechanical Properties of the Coatings

For each thin film, the characteristics of the contact area of a typical indent (for hardness evaluation) are shown in Figure 6. To add to it, the hardness, Young's modulus and hardness to Young's modulus ratios ( $H/E$  and  $H^3/E^2$ ) of thin films are summarized



in Table 3. The Young's modulus increases with the increasing substrate bias voltage. The other parameters ( $H$ ,  $H/E$  and  $H^3/E^2$ ) have a different trend, so at first, they increase (from S50 to S125), and then, they decrease (from S125 to S200). Moreover, as can be seen from Figure 6a'–c', it is clear that the deformed volume of S50 is maximum, whereas it is minimum for S125. Hence, it can be deduced that S125 has the maximum mechanical properties. Compared with the other Cr-N based thin film [1,3,22], S125 achieves higher levels of  $H/E$  and  $H^3/E^2$ .

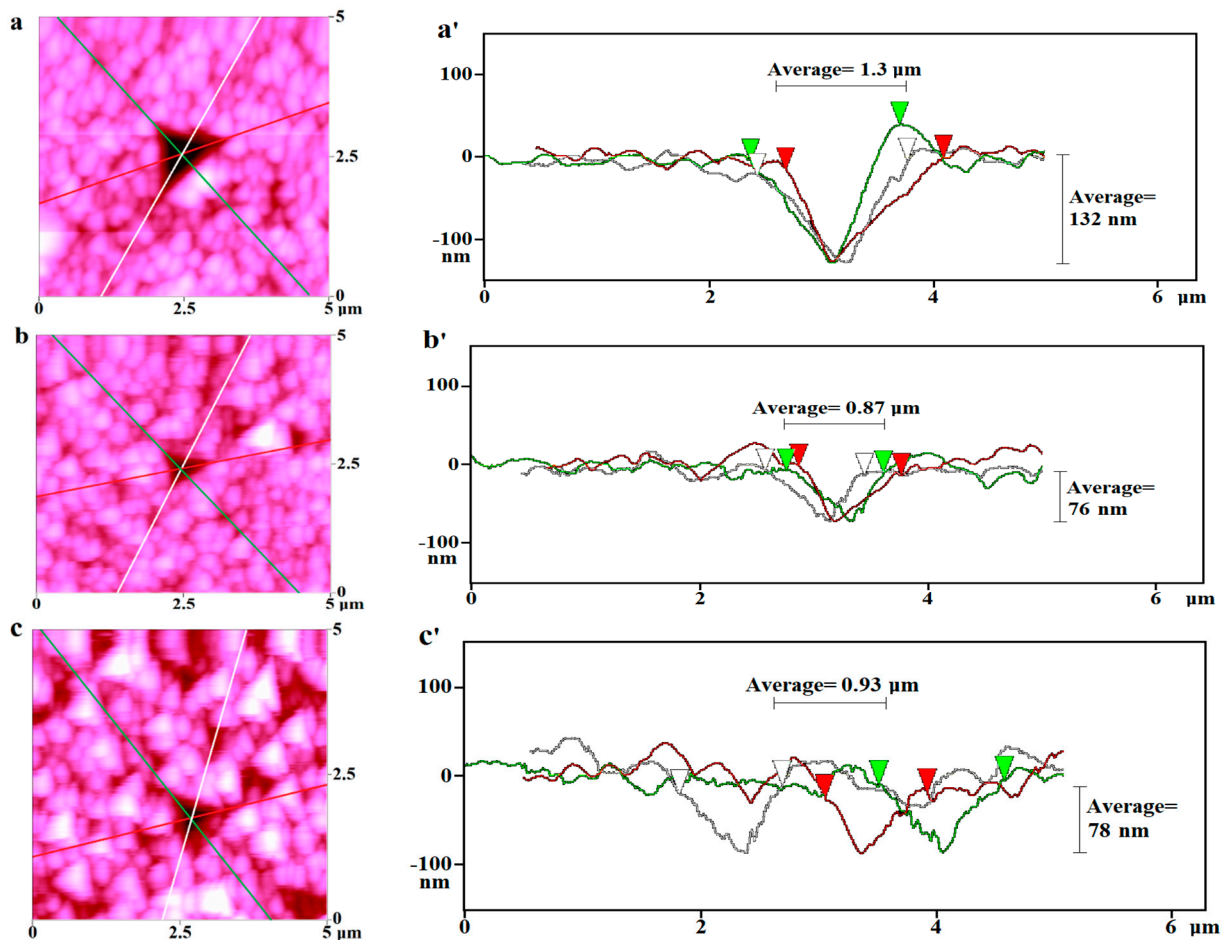


**Figure 6.** AFM images of indented area and cross-sectional profiles of thin films: (a,a') S50, (b,b') S125 and (c,c') S200.

**Table 3.** Hardness and toughness parameters of thin films.

Sample Code	H (GPa)	E (GPa)	H/E (-)	$H^3/E^2$ (GPa)
S50	$14.3 \pm 2.6$	$221.5 \pm 7.9$	0.064	0.059
S125	$24.5 \pm 1.1$	$228.9 \pm 5.1$	0.107	0.280
S200	$22.8 \pm 1.9$	$244.3 \pm 5.8$	0.093	0.198

To investigate the fracture behavior of Cr-Nb-Ti-Zr-N-O thin films, high load indentation (the load is 500 mN) is applied, and surface SEM images are presented in Figure 7. It is obvious that buckling, complete fracture and delamination occurred in S50. These low-quality fracture features have been seen for low-toughness thin films [48]. This behavior can be due to the minimum toughness characteristics ( $H/E$  and  $H^3/E^2$ ) of sample S50. There are micro-cracks in the samples of S125 and S200. The average length of these radial cracks is  $6.22 \mu\text{m}$  for S125 and  $7.5 \mu\text{m}$  for S200. In addition, the deformed areas of S50, S125 and S200 are  $398$ ,  $34.7$  and  $39.1 \mu\text{m}^2$ , respectively. Therefore, it is obvious

that substrate-coating adhesion is at the lowest level in the case of S50. By increasing the substrate bias voltage, the adhesion of coating at the substrate interface is improved in the cases of S125 and S200.

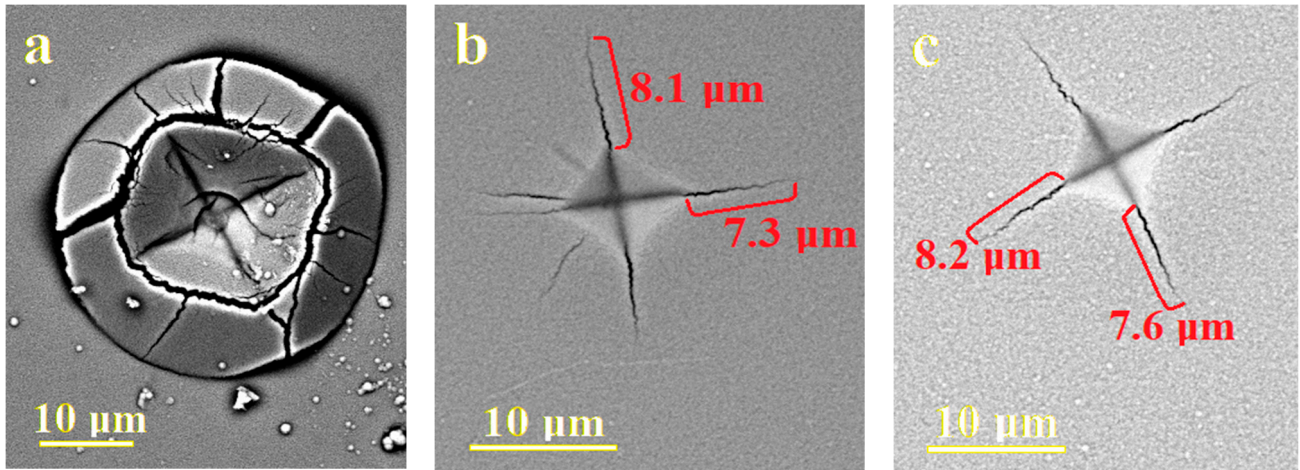


Figure 7. SEM images of Vickers indented area of thin films: (a) S50, (b) S125 and (c) S200.

The friction and worn area of Cr-Nb-Ti-Zr-N-O thin films (taken by nano-scratch test) are summarized in Figures 8 and 9. It is vivid that the friction behavior at the surface of the coatings is similar (the average friction coefficient of all samples is  $0.25 \pm 0.03$ ). However, there is a rupture (sudden decrease and increase) in the friction data of S50 and S200 (see pink circles in Figure 8). Moreover, the higher wear depth (more than 101 nm) can be observed in samples S50 and S200 (see Figure 9a',c'). A minimum wear width and depth were achieved in S125.

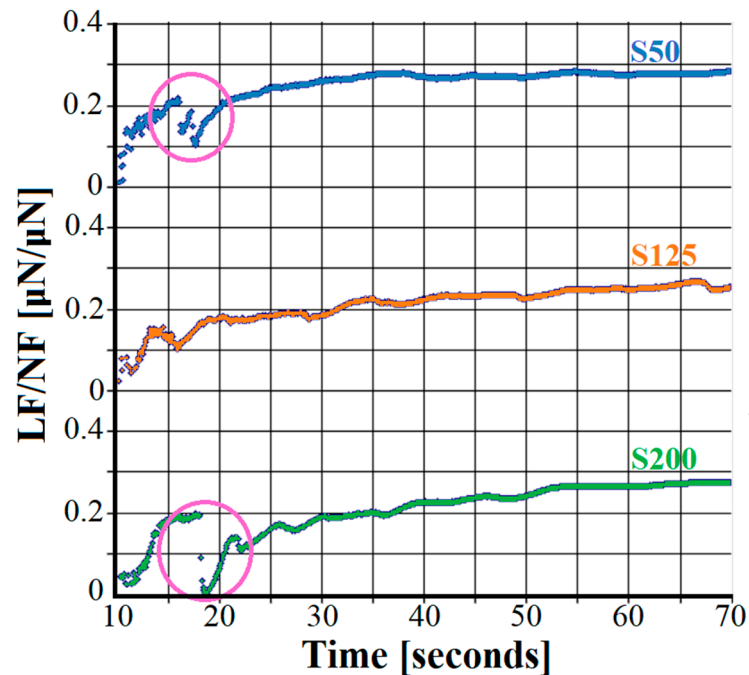
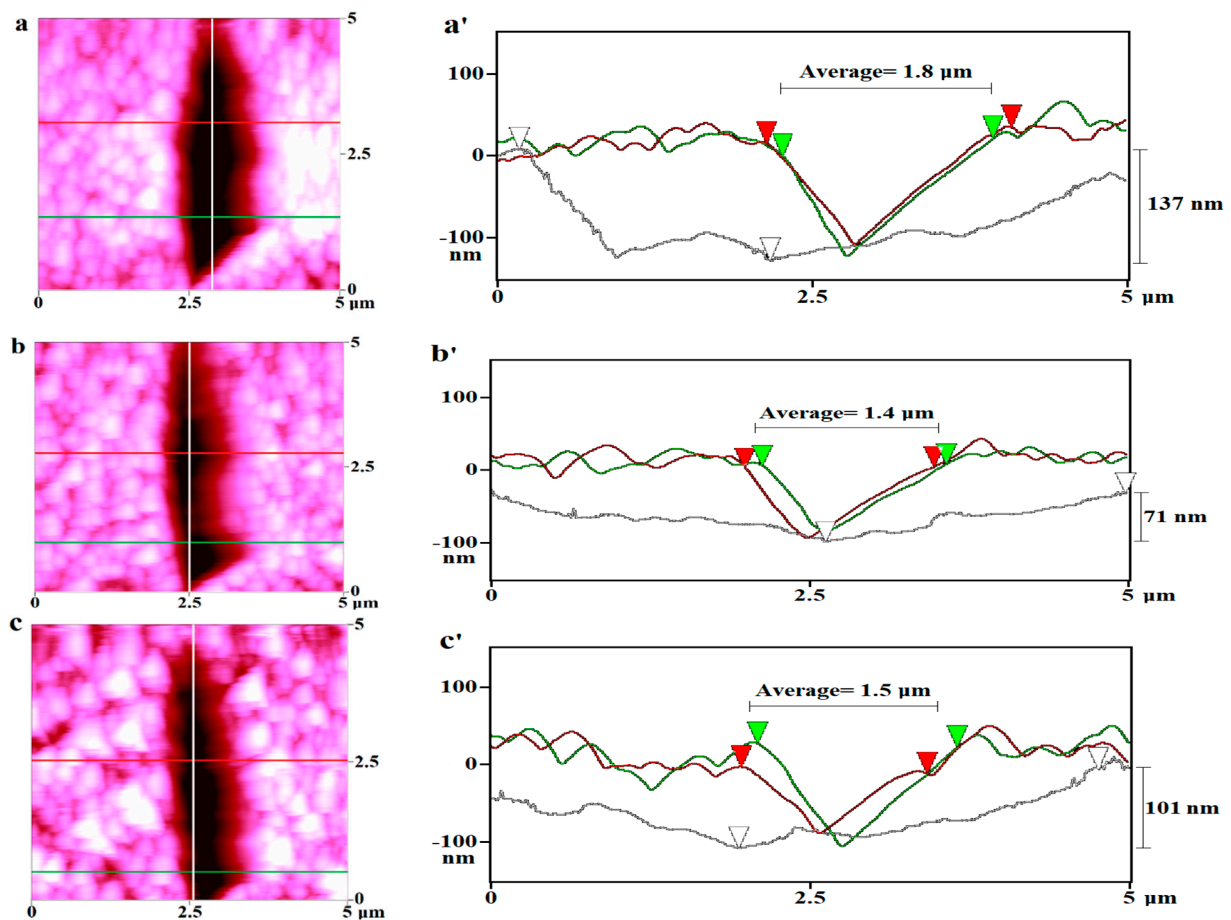


Figure 8. Friction coefficient (LF/NF) of thin films based on nano-scratch test.



**Figure 9.** AFM images of scratch area and cross-sectional profiles of thin films: (a,a') S50, (b,b') S125 and (c,c') S200.

#### 4. Discussion

According to the EDS results, it can be concluded that oxygen entered into the Cr-Nb-Ti-Zr-N thin films effectively. Hence, the oxide phase ( $\text{CrO}_2$ ) can be crystallized like the nitride phases ( $\text{Nb}_2\text{N}$ ,  $\text{Cr}_2\text{N}$  and  $\text{CrN}$ ) in an amorphous matrix. In low-level bias voltage (S50), the particle energy [39,44] is low so that the atoms/ions cannot go to the right sites at the crystalline lattice. Hence, the amount of nano-crystalline phases is low, and an amorphous phase is major. By increasing the bias voltage (S125 and S200), the crystallinity rises significantly (see XRD and Raman peak intensities and numbers in Figures 1 and 2). This trend was recorded in the other study [33] that worked on the bias voltage variation effect on the structure of multi-component ceramic film. Moreover, the morphology and topology of the coatings change remarkably by increasing the substrate voltage. So, the roughness, skewness and kurtosis levels decrease seriously in samples S125 and S200 (see Table 3). In addition, macro-particles (agglomerated particles on the surface of S50) can disappear in the cases of S125 and S200 (compare Figure 4a–c). This result is in accordance with the previous study of the authors [24]. However, because of the nature of the sputtering process, which can generate micro-voids [25,39], porosity/open boundaries are created in all samples (see Figure 3a'–c' and Figure 4a,c').

The variations in chemical and morphological characteristics have great effects on the mechanical properties of medium- and high-entropy ceramic coatings [1,14,15]. In the case of Cr-Nb-Ti-Zr-N-O thin films, adding Ti and O to the system of Cr-Zr-Nb-N can enhance the Young's modulus slightly. Furthermore, the sample with less crystalline content in an amorphous matrix (S50) has a lower hardness value (14.3 GPa) compared with the others. This discussion is in good agreement with the theory [8,27] that nanocomposite mi-

crostructures with a higher content and dispersity degree of reinforcement/nano-crystalline phase can cause higher hardness. Likewise, because of the higher content of defect density (34%, consisted of open boundaries and macro-particles) in S50, the hardness deviation from the average number is substantial ( $\pm 2.6$  GPa). Furthermore, to interpret the deformation/fracture behavior (the deformed area made by Vickers indent and crack length) and wear (scratch width and depth) parameters of Cr-Nb-Ti-Zr-N-O ceramic films, it is important to regard both aspects of thin films' chemistry and morphology. Therefore, two major mechanical properties (the deformed area extracted from Figure 7 and the wear depth extracted from Figure 9) of the coatings are presented in Figure 10 regarding their toughness parameter (H/E data from Table 3) and defect density percentage (from Section 3.2). As can be seen from Figure 10a, it is obvious that there is a descending trend in the case of H/E-deformed area and H/E-wear depth. It demonstrates that the higher toughness parameter of a thin film can cause higher resistance during static and dynamic indentation. This result was reported by others [3,42]. To add to it, it must be mentioned that defects can facilitate crack propagation, delamination and fracture. This is especially evident when there are micro-voids/columnar boundaries in the morphology of the coatings because they have low cohesive energy to propagate cracks [33,49]. To study this feature in samples S50, S125 and S200, Figure 10b shows the predictable trend (higher defect density can cause higher deformation and wear characteristics). The voids and boundaries among the large columns in samples S50 and S200 are the preferable paths to develop cracks, so material detachment amounts will be increased under static and dynamic loading. In addition, a high content of defects can create unusual friction behavior (sudden decrease–increase in friction coefficient data of S50 and S200; see Figure 8).

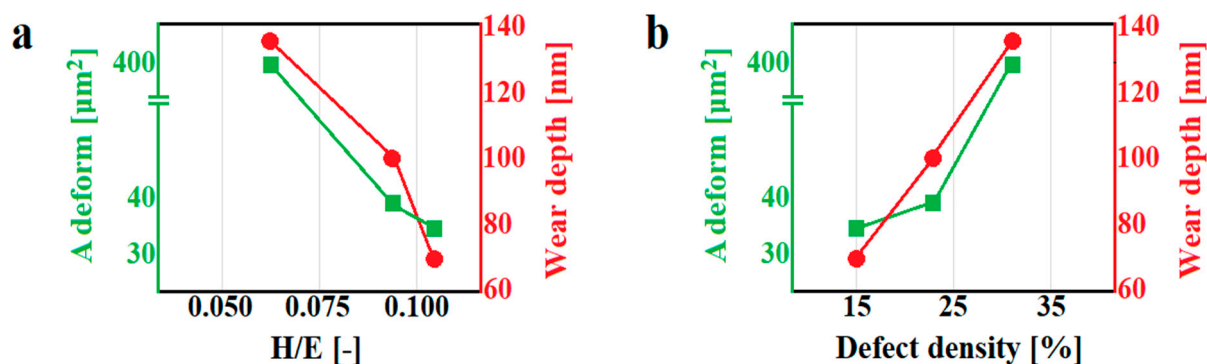


**Figure 10.** Effect of H/E (a) and defect (porosity + macroparticles) density (b) on deformation properties of thin films.

In the machining industries, it is important to apply a coating technology with high efficiency (high deposition rate with low energy consumption). At the same time, the process should bring low defect density in the structure of the coating. Therefore, according to this study, one can find the material system with high hardness (24.5 GPa in the case of S125) and toughness (H/E is more than 0.1 and  $H^3/E^2$  is more than 0.27) at the same time. Additionally, the optimum bias voltage ( $-125$  V) is found to obtain a nanocomposite coating with few defects. As Mitterer and his colleagues [7] proved, nanocomposite microstructure coatings with more than a single crystalline phase can enhance thermal stability. Hence, S125 (which has a defectless, nanocomposite and multi-phase structure) can be selected as an appropriate choice to use in various temperatures and industries (such as cutting tools and die machining).

## 5. Conclusions

Nanocomposite Cr-Nb-Ti-Zr-N-O ceramic films are produced by sputtering. The chemical, morphological and mechanical features of these films are studied comprehensively. All things considered, the following can be concluded:

- Under high voltage and temperature, oxygen can enter into thin films not only as an impurity but also as a principal element (according to EDS measurement, the oxygen atomic percentage in all thin films is more than 8.6%). This leads to the formation of the oxide crystalline phase (CrO<sub>2</sub>).
- Increasing the substrate bias voltage (from −50 to −125 V) during the deposition of Cr-Nb-Ti-Zr-N-O ceramic films can cause a defectless and uniform surface. However, by increasing the voltage more than this optimum level (such as in sample S200), the pores/open boundaries density will be raised.
- Ti and O can enhance the mechanical properties of thin films, because the hardness, Young's modulus and toughness (H/E) of Cr-Nb-Ti-Zr-N-O thin films are higher than the ones related to the Cr-Zr-Nb-N medium-entropy alloy coatings.
- To gain a wear-resistant coating (sample S125), it is important to achieve the minimum level of roughness (lower than 16.6 nm), skewness (0.2) and kurtosis (lower than 3).

**Author Contributions:** Conceptualization, S.A.A.; methodology, S.A.A. and S.M.Q.; formal analysis, S.A.A. and S.M.Q.; investigation, S.M.Q.; data curation, S.A.A.; writing—original draft preparation, S.A.A.; resources, M.R.Z.-M. and F.F.; writing—review and editing, M.R.Z.-M.; supervision, M.R.Z.-M. and F.F.; project administration, M.R.Z.-M. and F.F. All authors have read and agreed to the published version of the manuscript.

**Funding:** This research did not receive any specific grant from funding agencies in the public, commercial, or not-for-profit sectors.

**Institutional Review Board Statement:** Not applicable.

**Informed Consent Statement:** Not applicable.

**Data Availability Statement:** Not applicable.

**Acknowledgments:** This research is sponsored by national funds through FCT—Fundação para a Ciência e a Tecnologia, under the project UIDB/00285/2020 and LA/P/0112/2020.

**Conflicts of Interest:** The authors declare no conflict of interest.

## References

1. Lyu, L.; Yang, J.; Zhou, M.; Yan, M.; Yang, J. Microstructure, mechanical properties and lead-bismuth eutectic corrosion behavior of (AlCrFeTiMo)NO and (AlCrFeTiNb)NO high entropy metal sublattice ceramic coatings. *Vacuum* **2023**, *209*, 111774. [[CrossRef](#)]
2. Chang, L.; Tzeng, C.; Chen, Y. Effects of W Content on Structural and Mechanical Properties of TaWN Films. *Coatings* **2022**, *12*, 700. [[CrossRef](#)]
3. Tang, J.; Lin, C.; Yang, F.; Chang, C. Influence of Nitrogen Content and Bias Voltage on Residual Stress and the Tribological and Mechanical Properties of CrAlN Films. *Coatings* **2020**, *10*, 546. [[CrossRef](#)]
4. Yin, X.; Wu, S.; Dastan, D.; Nie, S.; Liu, Y.; Li, Z.; Zhou, Y.; Li, J.; Faik, A.; Shan, K.; et al. Sensing selectivity of SnO<sub>2</sub>-Mn<sub>3</sub>O<sub>4</sub> nanocomposite sensors for the detection of H<sub>2</sub> and CO gases. *Surf. Interfaces* **2021**, *25*, 101190. [[CrossRef](#)]
5. Bueno, C.; Maestre, D.; Díaz, T.; Juárez, H.; Pacio, M.; Cremades, A.; Piqueras, J. High-yield growth of Ti doped ZnO nano- and microstructures by a vapor-solid method. *J. Alloys Compd.* **2017**, *726*, 201–208. [[CrossRef](#)]
6. Rimmaudo, I.; Loeza-Poot, M.; Camacho-Espinosa, E.; Mis-Fernández, R.; Peña, J. Enhanced uniformity of sputtered oxygenated cadmium sulfide (CdS:O) films for large area photovoltaic applications. *Sol. Energy* **2018**, *173*, 1025–1031. [[CrossRef](#)]
7. Mitterer, C.; Mayrhofer, P.H.; Musil, J. Thermal stability of PVD hard coatings. *Vacuum* **2003**, *71*, 279–284. [[CrossRef](#)]
8. Musil, J.; Vlcek, J. Magnetron sputtering of hard nanocomposite coatings and their properties. *Surf. Coat. Technol.* **2001**, *142–144*, 557–566. [[CrossRef](#)]
9. Aissani, L.; Alhussein, A.; Wasy Zia, A.; Mamba, G.; Rtimi, S. Magnetron Sputtering of Transition Metal Nitride Thin Films for Environmental Remediation. *Coatings* **2022**, *12*, 1746. [[CrossRef](#)]
10. Glechner, T.; Hahn, R.; Wojcik, T.; Holec, D.; Koložsvári, S.; Zaid, H.; Kodambaka, S.; Mayrhofer, P.; Riedl, H. Assessment of ductile character in superhard Ta-C-N thin films. *Acta Mater.* **2019**, *179*, 17–25. [[CrossRef](#)]
11. Kindlund, H.; Sangiovanni, D.; Petrov, I.; Greene, J.; Hultman, L. A review of the intrinsic ductility and toughness of hard transition-metal nitride alloy thin films. *Thin Solid Film.* **2019**, *688*, 137479. [[CrossRef](#)]
12. Friedrich, A.; Winkler, B.; Juarez-Arellano, E.; Bayarjargal, L. Synthesis of Binary Transition Metal Nitrides, Carbides and Borides from the Elements in the Laser-Heated Diamond Anvil Cell and Their Structure-Property Relations. *Materials* **2011**, *4*, 1648–1692. [[CrossRef](#)] [[PubMed](#)]

13. Li, X.; Petrov, I.; Hultman, L.; Greczynski, G. Determining role of W<sup>+</sup> ions in the densification of TiAlWN thin films grown by hybrid HiPIMS/DCMS technique with no external heating. *J. Vac. Sci. Technol. A* **2023**, *41*, 013407. [[CrossRef](#)]
14. Yan, K.; Xian, G.; Zhao, H.; Fan, H.; Wang, J.; Wang, H.; Du, H. Effect of Mo content on the structure and mechanical properties of TiAlMoN films deposited on WC–Co cemented carbide substrate by magnetron sputtering. *Int. J. Refract. Met. Hard Mater.* **2015**, *52*, 29–35. [[CrossRef](#)]
15. Hu, C.; Xu, Y.; Chen, L.; Pei, F.; Zhang, L.; Du, Y. Structural, mechanical and thermal properties of CrAlNbN coatings. *Surf. Coat. Technol.* **2018**, *349*, 894–900. [[CrossRef](#)]
16. Hu, C.; Xu, Y.; Chen, L.; Pei, F.; Du, Y. Mechanical properties, thermal stability and oxidation resistance of Ta-doped CrAlN coatings. *Surf. Coat. Technol.* **2019**, *368*, 25–32. [[CrossRef](#)]
17. Jun Kim, D.; Min Kim, S.; Hyun La, J.; Yul Lee, S.; Sun Hong, Y.; Hyung Lee, M. Synthesis and characterization of CrZrAlN films using unbalanced magnetron sputtering with segment targets. *Met. Mater. Int.* **2013**, *19*, 1295–1299. [[CrossRef](#)]
18. Navinšek, B.; Panjan, P.; Cvelbar, A. Characterization of low temperature CrN and TiN (PVD) hard coatings. *Surf. Coat. Technol.* **1995**, *75*, 155–161. [[CrossRef](#)]
19. Mansoor, N.; Fattah-alhosseini, A.; Elmkhah, H.; Shishehian, A. Electrochemical behavior of TiN, CrN and TiN/CrN nanostructured coatings on the nickel-chromium alloy used in dental fixed prosthesis. *J. Asian Ceram. Soc.* **2020**, *8*, 694–710. [[CrossRef](#)]
20. Beltrami, M.; Mavrič, A.; Dal Zilio, S.; Fanetti, M.; Kapun, G.; Lazzarino, M.; Sbaizero, O.; Čekada, M. A comparative study of nanolaminate CrN/Mo<sub>2</sub>N and CrN/W<sub>2</sub>N as hard and corrosion resistant coatings. *Surf. Coat. Technol.* **2023**, *455*, 129209. [[CrossRef](#)]
21. Marques de Castilho, B.; de Sousa Mazuc, F.; Mendes Rodrigues, A.; Tavares Avila, P.; Chefer Apolinario, R.; Daum, P.; Pereira da Costa, F.; Rodrigues Menezes, R.; de Araújo Neves, G.; Greiner, C.; et al. Tailoring the Hybrid Magnetron Sputtering Process (HiPIMS and dcMS) to Manufacture Ceramic Multilayers: Powering Conditions, Target Materials, and Base Layers. *Nanomaterials* **2022**, *12*, 2465. [[CrossRef](#)]
22. Hones, P.; Sanjines, R.; Levy, F. Sputter deposited chromium nitride based ternary compounds for hard coatings. *Thin Solid Film.* **1998**, *332*, 240–246. [[CrossRef](#)]
23. Aouadi, S.; Maeruf, T.; Twesten, R.; Mihut, D.; Rohde, S. Physical and mechanical properties of chromium zirconium nitride thin films. *Surf. Coat. Technol.* **2006**, *200*, 3411–3417. [[CrossRef](#)]
24. Ataie, S.A.; Keshtmand, R.; Zamani-Meymian, M.R. Nano-mechanical properties of Cr-Zr-Nb-N medium entropy alloy films produced by reactive sputtering. *Int. J. Refract. Met. Hard Mater.* **2023**, *110*, 106006. [[CrossRef](#)]
25. Panjan, P.; Cekada, M.; Panjan, M.; Kek-Merl, D. Growth defects in PVD hard coatings. *Vacuum* **2009**, *84*, 209–214. [[CrossRef](#)]
26. Mei, H.; Cai, Z.; Ding, J.; Yan, K.; Li, Q.; Zhao, Z.; Zhao, J.; Cheng, L.; Liu, M.; Gong, W. The Additions of V and Cu on the Microstructure and Mechanical Properties of Mo-N Coatings. *Coatings* **2022**, *12*, 1129. [[CrossRef](#)]
27. Cavaleiro, A.; Louro, C. Nanocrystalline structure and hardness of thin films. *Vacuum* **2002**, *64*, 211–218. [[CrossRef](#)]
28. Pristáš, G.; Bačkai, J.; Orendáč, M.; Gabáni, S.; Košuth, F.; Kuzmiak, M.; Szabó, P.; Gažo, E.; Franz, R.; Hirn, S.; et al. Superconductivity in medium- and high-entropy alloy thin films: Impact of thickness and external pressure. *Phys. Rev. B* **2023**, *107*, 024505. [[CrossRef](#)]
29. Ataie, S.A.; Soltanieh, M.; Naghizadeh, R.; Ahmadi, M.; Ghanaatshoar, M. Effects of substrate temperature and reactive gas flow rate on the crystalline ceramic phases formation and tribological properties of W–Ti–Co–C–N thin films produced by co-sputtering. *Ceram. Int.* **2020**, *46*, 29137–29149. [[CrossRef](#)]
30. Kumada, T.; Ohtsuka, M.; Fukuyama, H. Influence of substrate temperature on the crystalline quality of AlN layers deposited by RF reactive magnetron sputtering. *AIP Adv.* **2015**, *5*, 017136. [[CrossRef](#)]
31. Ferreira, F.; Cavaleiro, A.; Oliveira, J. Tribological performance of DLC coatings deposited by DOMS in mixed Ar-Ne discharges. *Mater. Lett.* **2021**, *285*, 129056. [[CrossRef](#)]
32. Dastan, D.; Shan, K.; Jafari, A.; Gity, F.; Yin, X.; Shi, Z.; Alharbi, N.; Ahmad Reshi, B.; Fu, W.; Țălu, S.; et al. Influence of nitrogen concentration on electrical, mechanical, and structural properties of tantalum nitride thin films prepared via DC magnetron sputtering. *Appl. Phys. A* **2022**, *128*, 400. [[CrossRef](#)]
33. Ataie, S.A.; Soltanieh, M.; Naghizadeh, R.; Cavaleiro, A.; Evaristo, M.; Fernandes, F.; Ferreira, F. Effect of substrate bias voltage on structural and tribological properties of W-Ti-C-N thin films produced by combinational HiPIMS and DCMS co-sputtering. *Wear* **2023**, *520–521*, 204654. [[CrossRef](#)]
34. Ferreira, F.; Cavaleiro, A.; Oliveira, J. Effect of substrate biasing on the structure and properties of tantalum coatings deposited using HiPIMS in deep oscillation magnetron sputtering mode. *Metals* **2020**, *10*, 1618. [[CrossRef](#)]
35. Yang, Z.; Yang, B.; Guo, L.; Fu, D. Effect of bias voltage on the structure and hardness of TiSiN composite coatings synthesized by cathodic arc assisted middle-frequency magnetron sputtering. *J. Alloys Compd.* **2009**, *473*, 437–441. [[CrossRef](#)]
36. Sert, Y.; Küçükömeroğlu, T.; Efeoğlu, I. Investigating the structure, adhesion and tribological properties of Al and Zr-doped TiN coatings with various substrate bias voltage and working pressure. *Proc. Inst. Mech. Eng. Part J J. Eng. Tribol.* **2020**, *235*, 6. [[CrossRef](#)]
37. Ferreira, F.; Serra, R.; Oliveira, J.; Cavaleiro, A. Effect of peak target power on the properties of Cr thin films sputtered by HiPIMS in deep oscillation magnetron sputtering (DOMS) mode. *Surf. Coat. Technol.* **2014**, *258*, 249–256. [[CrossRef](#)]
38. Zhang, S.; Sun, D.; Fu, Y.; Du, H. Effect of sputtering target power on microstructure and mechanical properties of nanocomposite nc-TiN/a-SiN<sub>x</sub> thin films. *Thin Solid Film.* **2004**, *447–448*, 462–467. [[CrossRef](#)]

39. Thornton, J.A. The microstructure of sputter-deposited coatings. *J. Vac. Sci. Technol. A* **1986**, *4*, 3059–3065. [[CrossRef](#)]
40. Bavadi, R.; Valedbagi, S. Physical properties of titanium nitride thin film prepared by DC magnetron sputtering. *Mater. Phys. Mech.* **2012**, *15*, 167–172.
41. Valvoda, V.; Černý, R.; Kužel, R., Jr.; Musil, J.; Poulek, V. Dependence of microstructure of TiN coatings on their thickness. *Thin Solid Film.* **1988**, *158*, 225–232. [[CrossRef](#)]
42. Musil, J.; Poláková, H. Hard nanocomposite Zr–Y–N coatings, correlation between hardness and structure. *Surf. Coat. Technol.* **2000**, *127*, 99–106. [[CrossRef](#)]
43. Aliramaji, S.; Keuter, P.; Neuß, D.; Hans, M.; Primetzhofer, D.; Depla, D.; Schneider, J. Effect of Growth Temperature and Atmosphere Exposure Time on Impurity Incorporation in Sputtered Mg, Al, and Ca Thin Films. *Materials* **2023**, *16*, 414. [[CrossRef](#)] [[PubMed](#)]
44. Adjaottor, A.A.; Meletis, E.I.; Logothetidis, S.; Alexandrou, I.; Kokkou, S. Effect of substrate bias on sputter-deposited TiCx, TiNy and TiCxNy thin films. *Surf. Coat. Technol.* **1995**, *76–77*, 142–148. [[CrossRef](#)]
45. Vuurman, M.A.; Wachs, I.E. In situ Raman spectroscopy of alumina-supported metal oxide catalysts. *J. Phys. Chem.* **1992**, *96*, 5008–5016. [[CrossRef](#)]
46. Kotwal, C.A.; Bhushan, B. Contact analysis of non-Gaussian surfaces for minimum static and kinetic friction and wear. *Tribol. Trans.* **1996**, *39*, 890–898. [[CrossRef](#)]
47. Zamani-Meymian, M.R.; Abdolvahab, R.H.; Mehr, A. Fractal characteristics of TiO<sub>2</sub>-Ag nanocomposite films deposited by a grid-assisted co-sputtering method. *Appl. Surf. Sci.* **2019**, *480*, 593–600. [[CrossRef](#)]
48. Zhang, S.; Sun, D.; Fu, Y.; Du, H. Toughness measurement of thin films: A critical review. *Surf. Coat. Technol.* **2005**, *198*, 74–84. [[CrossRef](#)]
49. Meindlhumer, M.; Ziegelwanger, T.; Zalesak, J.; Hans, M.; Lofler, L.; Spor, S.; Jager, N.; Stark, A.; Hruby, H.; Daniel, R.; et al. Precipitation-based grain boundary design alters inter- to trans-granular fracture in AlCrN thin films. *Acta Mater.* **2022**, *237*, 118156. [[CrossRef](#)]

**Disclaimer/Publisher’s Note:** The statements, opinions and data contained in all publications are solely those of the individual author(s) and contributor(s) and not of MDPI and/or the editor(s). MDPI and/or the editor(s) disclaim responsibility for any injury to people or property resulting from any ideas, methods, instructions or products referred to in the content.